Intelligent Process Monitoring of Laser-Induced Graphene Production with Deep Transfer Learning

Min Xia, *Senior Member, IEEE*, Haidong Shao, Zheng Huang, Zhe Zhao, Feilong Jiang, and Yaowu Hu

Abstract—**Three-dimensional (3D) graphene has been increasingly used in many applications due to its superior properties. The laser-induced graphene (LIG) technique is an effective way to produce 3D graphene by combining graphene preparation and patterning into a single step using direct laser writing. However, the variation in process parameters and environment could largely affect the formation and crystallization quality of 3D graphene. This paper develops a vision and deep transfer learning-based processing monitoring system for LIG production. To solve the problem of limited labeled data, novel convolutional de-noising auto-encoder (CDAE)-based unsupervised learning is developed to utilize the available unlabeled images. The learned weights from CDAE are then transferred to a gaussian convolutional deep belief network (GCDBN) model for further fine-tuning with a very small amount of labeled images. The experimental results show the proposed method can achieve the state-of-art performance of precise and robust monitoring for the quality of the LIG formation.**

Index Terms—**Laser-induced graphene, process monitoring, deep transfer learning, semi-supervised learning.**

I. Introduction

Since the discovery of graphene by Andre Geim, it has been widely used in microelectronics [1], energy storage[2], composite materials[3], and bionic devices [4]. In practical applications, for example, as an electrode material for energy storage and conversion devices, the two-dimensional (2D) graphene layer tends to re-stack and lose its unique properties, resulting in unsatisfactory performance [5]. An effective way to solve this issue is to construct graphene into a well-organized and interconnected three-dimensional (3D) structure, which not only retains the excellent properties of 2D graphene, but also shows a low mass density (~0.16 mg/cm^3), high porosity, large specific surface area and unexceptionable flexibility [6].

At present, 3D graphene-based materials mainly include graphene hydrogels, graphene sponges, graphene aerogels, and graphene foams. Generally, the production of 3D graphene macrostructures includes methods such as self-assembly [7], template-assisted synthesis [8], and direct deposition [9]. However, the traditional manufacturing method of 3D graphene

usually requires multiple steps to realize the construction of a 3D structure, such as graphene oxide (GO) synthesis, assembly of 3D structure, and reduction of GO. At the same time, various chemical reagents are needed in the manufacturing process, which is easy to cause environmental pollution. For industrial applications, traditional manufacturing methods are difficult to achieve large-area rapid manufacturing. Due to its high production efficiency and the ability to form micro-nano structures, laser-assisted processing technology has been widely used in material manufacturing. Recently, James M. Tour et al. confirmed that the use of commercially available CO2 infrared laser scribing could form 3D porous graphene on polyimide (PI) under ambient conditions [10]. Compared with the traditional preparation method, this method simplifies the preparation process, and the construction of 3D graphene can be completed by only one step of laser scanning. The manufacturing process does not require the use of chemical reagents and is environmentally friendly. At the same time, the laser manufacturing method can be easily combined with numerical control technology to realize automated and rapid manufacturing. Recently, a simple lamination composite method has been used to produce functional, patterned, and multilayer laser-induced graphene (LIG) composites, which is compatible with roll-to-roll processing [11].

In the manufacturing process of LIG, the changes of various process parameters and processing environment will affect the formation and crystallization quality of 3D graphene. So, the property of the final project needs to be confirmed by micro Raman spectrometer and other testing methods offline, which is time-consuming and effective in industrial production. The real-time monitoring technology plays a significant role in the field of laser-aided manufacturing. Establishing the mapping between real-time monitoring data and the properties of the products, not only ensures the product quality but also saves time and expenditure on the subsequent inspection. For example, Fraser et al. [12] used a low-coherence interferometric imaging technique to monitor melt pool morphology changes and stability during the selective laser melting process, which can detect process defects caused by poor parameter selections and identify characteristic fault signatures. Wong et al. [13] studied the correlation between micro-hardness of molten zone and the intensity of emission spectra were researched using the emission spectra detected during the laser melting process. However, for LIG production, effective process monitoring has not been investigated yet.

Recently, deep learning has shown promising capability in achieving effective process monitoring of laser aided manufacturing. Shevchik et al. [14] developed a deep

learning-based real-time quality monitoring system for power-bed fusion (PBF) additive manufacturing (AM) using acoustic emission signals. Various quality categories with different levels of porosity could be accurately classified using a spectral convolutional neural network. Eschner et al. [15] proposed an approach for specimen density classification using artificial neural networks and acoustic emissions during the PBF process. The ANN model established a precise linkage between density and acoustic signals. Image-based approaches have gained increasing attention in processing monitoring due to both the convenience of the use of cameras and the abundant information contained in images during the process [16]. Wang et al. [17] developed a vision-based surface monitoring system using convolutional neural network (CNN) for fused deposition modeling which could achieve efficient defect classification with high accuracy. Zhang et al. [18] used machine vision and hybrid CNN to classify the different defects in the PBF process. The hybrid CNN model could learn both the spatial and temporal representative features from the raw images automatically based on the advantages of the CNN architecture. Li et al. [19] proposed a deep learning-based process monitoring method for directed energy deposition in AM using thermal images collected during manufacturing. Feng et al. [20] developed a deep learning enhanced approach to improve gas tungsten arc welding process monitoring and penetration detection using multisource sensing images.

Despite the computer vision and deep learning-based methods can more effectively analyze and classify the manufacturing quality, they require a large number of labeled images to train the models from scratch [21]. However, In engineering practice, collecting and labeling large quantities of image samples with degraded performance of LIG production are usually laborious and even impractical. Unsupervised initialization combined with parameter transfer learning can provide powerful tools to handle this challenge [22]. With the unlabeled monitoring data that is typically easy to collect, a pre-trained unsupervised learning model can be used to initialize the deep learning model by transferring the parameters. In this paper, an in-situ process monitoring approach based on deep transfer learning is developed for LIG production. A high-speed camera is used to collect the images during the process. The experimental results show that the proposed approach can effectively evaluate the quality of 3D graphene produced with the in-process images. The main contributions of the paper are summarized as follows:

1. A vision and deep transfer learning-based process monitoring approach is developed for LIG production for the first time, which achieves precise evaluation of the formation.

2. The proposed method fully utilizes the unlabeled images collected by using a novel convolutional de-noising auto-encoder (CDAE) model.

3. With weight transfer learning from the novel CDAE to the Gaussian CDBN, only a small amount of labeled images are needed to achieve precise process monitoring.

The rest of the paper is organized as follows. Section II introduces the experimental setup of the developed vision-based LIG process monitoring system. Section III explains the principle of CDAE. The details of the proposed method are presented in Section IV. An experimental study, evaluation of the results, and discussion are presented in Section V. Section VI concludes this paper and highlights the future work.

II. EXPERIMENTAL SETUP

The developed vision-based LIG process monitoring system is shown in **Fig. 1**. Thermosetting polyimide (PI) solutions were coated to the surface of the substrate by knife coating method. A CO_2 laser cutting system with a wavelength of 10.6 um was used to directly synthesise graphene on the PI films under ambient conditions. The laser scanning speed was 150mm/s. The laser head was 2cm above the PI film. The in-process images of the manufacturing process were collected utilizing CHRONOS high-speed camera. The frame rate of the high-speed camera was set to 2111 fps and the image resolution was 1280*512. The camera was fixed with a tripod and was 30 cm away from the sample surface. Auxiliary LED was used as the fill light for the high-speed camera.
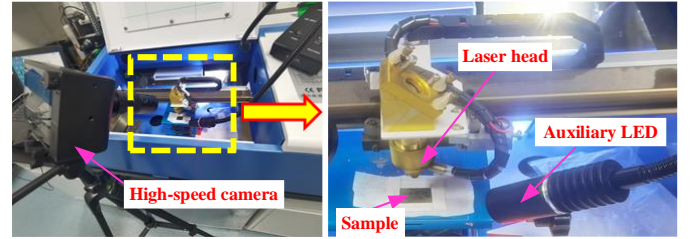

Fig.1. Vision-based process monitoring system of LIG production.

Different levels of laser power including 7%, 8%, 10.5%, 11%, and 15% were used to produce different formations. Raman spectra of LIG were obtained by excitation with a 532nm laser in Zolix RTS2 Micro confocal Raman spectrometer system with a 50x objective lens. The optical photograph of the sample was obtained with an Olympus BX35 microscope. The MIRA 3 field emission scanning electron microscope was used to obtain the micro morphology of the sample at 10 kV. Based on the Raman spectrum and micro morphology of the laser manufacturing results, the corresponding LIG formation categories are: (a) No formation; (b) Graphite formed; (c) Graphite and graphene; (d) Graphene formed; (e) Graphene destroyed. The processing parameters and the resulting formation categories are shown in Table I.

The objective of the experiment is to classify the five resulting formations by using the information from the in-process images, where most of the images are without formation categorical labels.

TABLE I
THE PROCESS PARAMETERS AND LIG FORMATION CATEGORIES

Formation Category	Laser Power (%)	Laser Scanning Speed (mm/s)
No formation	7	150
Graphite formed	8	150
Graphite and graphene	10.5	150
Graphene formed	11	150
Graphene destroyed	15	150

III. THE PRINCIPLE OF CONVOLUTIONAL AUTO-ENCODER

Different from CNN, convolutional de-noising auto-encoder

(CDAE) belongs to unsupervised learning algorithms. Unlike DAE, CDAE is constructed with 2D structure. Therefore, with the successful combination of CNN and DAE, CDAE can directly learn the useful characteristics of the 2D input in a completely unsupervised way [23]. Concretely, the encoder and decoder of the CDAE are built with convolution network and deconvolutional network, respectively, shown in **Fig. 2**.
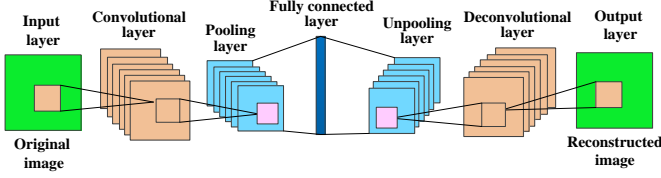

Fig. 2. The structure of a CDAE model.

The encoder is formed by an input layer, a convolution layer, and a pooling layer. Given an original 2D image x with no label in the input layer and its size is $N_V \times N_V$. The feature transformation process is expressed by

$$\hat{x} = x + N(0, \delta^2 I) \tag{1}$$

$$\hat{h}^k = \varphi(\hat{x} * W^k + b^k) \tag{2}$$

where $\hat{x}$ denotes the noisy 2D image, $N(0, \delta^2 I)$ denotes the Gaussian noise with zero mean and $\delta^2 I$ variance, I is the unit matrix, $\hat{h}^k$ denotes the kth hidden feature map with 2D size of $N_H \times N_H$, W^k denotes the weight matrix of the kth convolution kernel with 2D size of $N_W \times N_W$, $*$ denotes the 2D convolution operation, b^k denotes the bias of $\hat{h}^k$ and $\varphi(\cdot)$ denotes the transform function, usually selected as sigmoid. After the convolution layer, a max pooling layer with 2D size of $N_P \times N_P$ is added to reduce feature dimensionality.

An unpooling layer, a deconvolutional layer, and an output layer constitute the decoder, which aims at reconstructing the original input from the hidden feature map as

$$\hat{y} = \varphi\left(\sum_{k=1}^{K} \hat{h}^k * \tilde{W}^k + c\right) \tag{3}$$

where $\tilde{W}^k$ denotes the weight matrix of the kth deconvolution kernel, which is the flip of W^k, K denotes the number of the hidden feature maps, c denotes the bias of decoder, and $\hat{y}$ denotes the reconstruction of input. Before the deconvolutional layer, an unpooling layer should be added for recovering the original 2D size. By minimizing the mean square error (MSE) between the input and reconstruction, the weight parameters of CDAE can be updated with stochastic gradient descent (SGD) optimization algorithm, expressed as

$$[W^k]_{(T+1)} = [W^k]_{(T)} - \eta \frac{\partial [L_{CAE}]_{(T+1)}}{\partial [W^k]_{(T+1)}} \tag{4}$$

$$L_{CAE} = \frac{1}{2N} \sum_{i=1}^{N} (x^{(i)} - \hat{y}^{(i)})^2 \tag{5}$$

where η denotes the learning rate, N denotes the number of the 2D image samples that all have no labels, $x^{(i)}$ denotes the ith image sample, T denotes the current iteration, $[W^k]_{(T)}$ and $[L_{CAE}]_{(T)}$ denote the trained weight and MSE at the Tth iteration, respectively;

IV. THE PROPOSED METHOD

A. Gaussian CDBN construction

Convolutional deep belief network (CDBN) is a new-type deep learning model which combines advantages of DBN and CNN. In terms of structure, CDBN is more similar to CNN than DBN, which has the ability to use the two-dimensional structure of images, and also has the characteristics of weight sharing and local receptive field. In terms of principle, CDBN is more similar to DBN than CNN, which belongs to a hierarchical generative model and adopts unsupervised layer-by-layer greedy pre-training algorithm. However, the traditional CDBN constructed with binary units in both the visible (input) and hidden layers is not ideal for feature extraction and classification of the collected images from the high-speed camera. By employing Gaussian units instead of binary ones, the so-called Gaussian DBN has shown obvious advantages in dealing with real-valued images, such as non-binary images with noise [24, 25]. Accordingly, Gaussian CDBN (GCDBN) is built in this paper based on Gaussian input units and hidden units. Concretely, GCDBN is composed of multiple base models named Gaussian Convolutional Restricted Bozeman Machine (GCRBM) with the new energy function as

$$E(v, h) = \frac{1}{2} \sum_{i,j=1}^{N_V} v_{i,j}^2 + \frac{1}{2} \sum_{k=1}^{K} \sum_{i,j=1}^{N_H} (h_{i,j}^k)^2$$
$$- \sum_{k=1}^{K} \sum_{i,j=1}^{N_H} \sum_{r,s=1}^{N_W} h_{i,j}^k W_{r,s}^k v_{i+r-1, j+s-1}$$
$$- \sum_{k=1}^{K} b^k \sum_{i,j=1}^{N_H} h_{i,j}^k - a \sum_{i,j=1}^{N_V} v_{i,j} \tag{6}$$

where v and h denote the Gaussian input layer and hidden layer, respectively, v accepts the non-binary 2D images with a size of $N_W \times N_W$, h has K feature maps denoted as $h^1, h^2, \ldots, h^K$ with each size of $N_H \times N_H$, and each feature map is linked to a weight matrix, successively denoted as $W^1, W^2, \ldots, W^K$, with each size of $N_W \times N_W$, $N_W = N_V - N_H + 1$, $v_{i,j}$ denotes the ith row and the jth column of v, $h_{i,j}^k$ denotes the ith row and the jth column of the kth feature map h^k, $W_{r,s}^k$ denotes the rth row and the sth column of the kth filter weight W^k, b^k denotes the bias, and a denotes the shared bias of all the input units.

In the GCDBN, a max pooling layer is added after the hidden layer to reduce features, which also has K groups with each size of $N_P \times N_P$, as shown in **Fig. 3**.

According to the new energy function, the conditional probabilities of the GCRBM for the input and hidden units are

$$P(h^k = I | v) = \mathcal{N}((\tilde{W}^k * v) + b^k, I) \tag{7}$$

$$P(v = I | h) = \mathcal{N}(\sum_k (W^k * h^k) + a, I) \tag{8}$$

where $\mathcal{N}(\mu, \sigma^2)$ denotes the Gaussian probability density function with mean μ and variance σ^2. The upgraded gradients with respect to the weights of GCRBM using contrastive divergence algorithm are expressed as

$$\Delta W_{r,s}^{k} = \eta \left(\left\langle \sum_{i,j=1}^{N_H} h_{i,j}^{k} v_{i+r-1,j+s-1} \right\rangle_{d} - \left\langle \sum_{i,j=1}^{N_H} h_{i,j}^{k} v_{i+r-1,j+s-1} \right\rangle_{m} \right) \qquad (9)$$

where, $<\cdot>_{d}$ and $<\cdot>_{m}$ denote the expectation over the data and model distributions, respectively, in which the latter can be efficiently estimated using one-step Gibbs sampling technique.

Despite the GCDBN can more effectively analyze and classify non-binary images with noise, its performance is significantly affected by the size of available labeled image samples. Obtaining a large number of labeled data is laborious or even impractical in a real application. In this study, unsupervised initialization combined with parameter transfer learning is used by transferring the parameter knowledge from a pre-trained unsupervised learning model to initialize the GCDBN. The next subsection introduces the weight parameter transfer between the novel CDAE and GCDBN in detail.
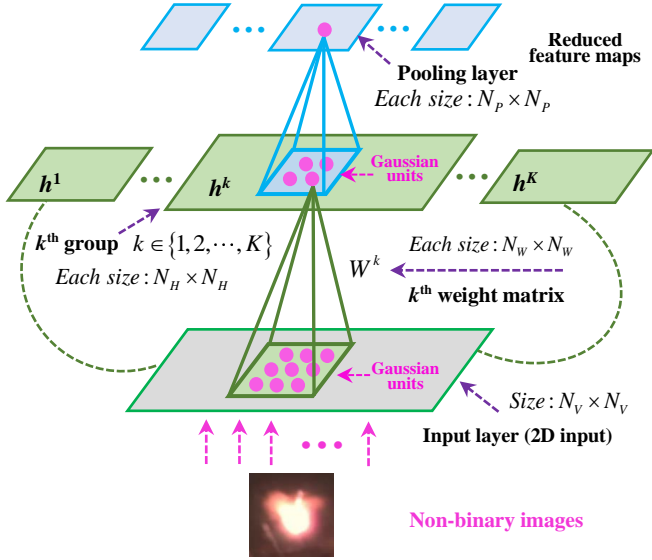

Fig. 3. The structure of a Gaussian CRBM model.

B. Novel CDAE design and weight transfer strategy

The key task of the CDAE model is to train the connection weights. According to the basic update rule shown in Eq. (4), it can be observed that only the weights after the previous iteration are used to update the current weights. Besides, the learning rate is fixed during the whole update process. These two problems are likely to lead to high oscillation and slow convergence of MSE. In order to simultaneously address the two problems mentioned above, adjustable learning rate and weight smoothing based on exponential moving average are combined and developed. Then, the new update rule for the weight is

$$\begin{cases} [\boldsymbol{W}^{k}]_{(T+1)} = [\boldsymbol{W}^{k}]_{(T)} - [\eta]_{(T+1)} \times [\partial L_{CAE} / \partial \boldsymbol{W}^{k}]_{(T+1)} \\ [\boldsymbol{W}^{k}]_{(T+1)} \leftarrow \dfrac{2 \times [\boldsymbol{W}^{k}]_{(T+1)} + T \times [\boldsymbol{W}^{k}]_{(T)}}{T+2}, \ T \geq 1 \end{cases} \qquad (10)$$

$$[\eta]_{(T)} = [\eta]_{(0)} \Big/ \sqrt{\sum_{i=1}^{T} ([g]_{(i)})^2 + \lambda} \qquad (11)$$

$$[g]_{(T)} = \frac{\partial [L_{CAE}]_{(T)}}{\partial [\boldsymbol{W}^{k}]_{(T)}} \qquad (12)$$

where $[\eta]_{(0)}$ denotes initial learning rate, λ denotes a very small positive number, $[\eta]_{(T)}$ and $[g]_{(T)}$ denote the learning rate and gradient at the Tth iteration, respectively.

From Eqs. (10)-(12), it can be found that (1) all of the trained weights from the previous iterations are utilized for further adjusting the present weight. (2) The contribution proportions of weights are different at the different iterations, specifically, the contribution from the weights in the latest iterations is higher than the weights in the early stage. (3) The learning rate can be adjusted according to the change of the gradient in real time, largely improving the training performance. These will make the learned weights smoother and the MSE curve converge more quickly.

By now, a novel CDAE has been designed. Compared with the labeled image samples, the unlabeled images are easier to be acquired, which can be fully used to train the novel CDAE with excellent performance. Then, the trained weights of the novel CDAE are transferred to the GCDBN with the same model structure as its initial weights. **Fig. 4** shows the main idea of weight transfer learning from novel CDAE to GCDBN. With the help of the initial weights containing good knowledge for pattern classification, the GCDBN can be efficiently trained with a very small number of labeled samples.
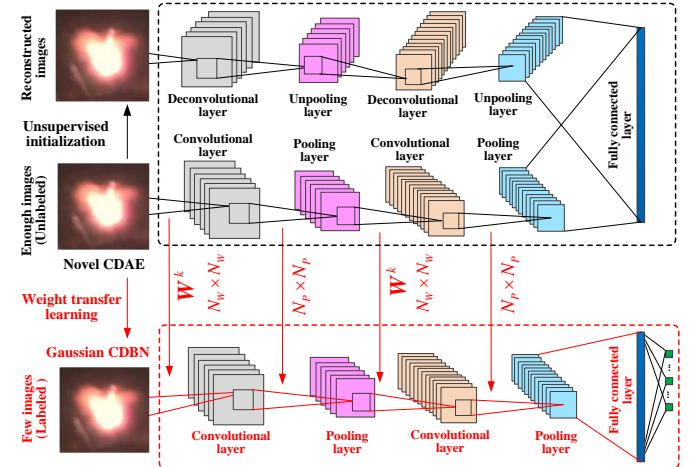

Fig. 4. Weight transfer learning from the novel CDAE to Gaussian GCDBN.

C. Framework of the proposed method

The implementation framework of process monitoring of LIG production in the proposed method is presented in **Fig. 5.** The main steps are summarized as follows:

Step 1: Collect the in-process images of LIG production under different conditions using a high-speed camera.

Step 2: Obtain the Raman spectra and micro morphology of some samples and determine the formation categories. Only a small number of samples are characterized and labeled with categorical information.

Step 3: Novel CDAE is constructed with adjustable learning rate and weight smoothing, which is used to learn the discriminative features from all the unlabeled images, and finally the trained weights containing good knowledge for pattern classification are acquired.

Step 4: Construct GCDBN by employing real-valued input units and hidden units, whose network structure is the same as the trained novel CDAE.

Step 5: The trained weights of the novel CDAE are transferred to the GCDBN as the initial weights.

Step 6: The small number of labeled images is used to further adjust the weights of the GCDBN to achieve high and robust classification performance.
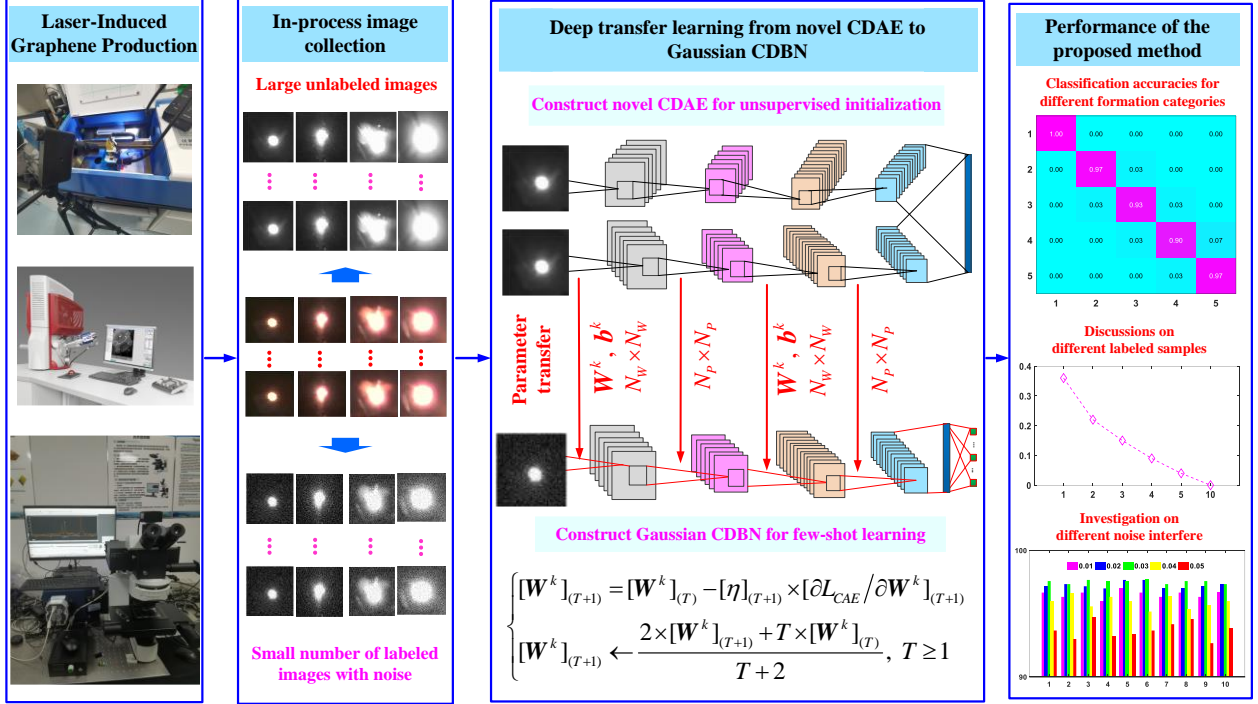

Fig. 5. The framework of the proposed method.

V. RESULTS AND DISCUSSION

A. In-process image collection and sample characterization

Five groups of image samples corresponding to the five LIG formation categories were collected using the developed system with laser power of 7%, 8%, 10.5%, 11%, and 15%. The samples sizes of the images for the five categories are listed in **Table II**. The number of the testing image samples is always fixed as 30. All of the unlabeled and labeled images are collected from the same process parameters and environment. One image sample cropped with only the region of interest from each of the five categories is shown in **Fig. 6**. The corresponding Raman spectrum and micro morphology are displayed in **Fig. 7**.

TABLE II
THE FIVE LIG FORMATION CATEGORIES AND THEIR SAMPLE SIZES

LIG formation categories	Unlabeled images for training novel CDAE	Labeled images for training/testing GCDBN	State labels
No formation	100	3 / 30	1
Graphite formed	100	3 / 30	2
Graphite and graphene	100	3 / 30	3
Graphene	100	3 / 30	4
Graphene destroyed	100	3 / 30	5

Fig. 6. The region of interest of the in process images for different categories: (a) State 1; (b) State 2; (c) State 3; (d) State 4; (e) State 5.

B. Effectiveness of the weight transfer based on unsupervised initialization

The effectiveness of the weight transfer strategy based on unsupervised initialization is first evaluated. As listed in **Table III**, the average testing accuracies during the ten independent runs of different combinations are compared. Specifically, Methods 1-6 adopt a weight transfer strategy based on unsupervised initialization, i.e., unlabeled image samples are firstly used for training the novel CDAE to get good weights for subsequent classifiers (such as Gaussian CDBN, Binary CDBN, and CNN), and then a few labeled image samples (three in this study) are used to further fine-tune the weights. On contrary, Methods 7-15 directly use different numbers of labeled image samples (50, 100, and 200) to train the classifiers from scratch. The average testing accuracy of Method 1 (the proposed method) is 95.40% (1431/1500), which is the highest among Methods 1-5. For one run, the multi-class confusion matrix is shown in **Fig. 8**, and the F-scores are 1, 0.9667, 0.9333, 0.9153, and 0.9508, respectively.

TABLE III
AVERAGE TESTING ACCURACIES OF DIFFERENT METHODS

Different methods	Sizes of unlabeled training samples for unsupervised initialization	Sizes of labeled samples for training	Average testing accuracies
Method 1 (Novel CDAE + Gaussian CDBN)	**100 * 5 for novel CDAE**	**3 * 5 for Gaussian CDBN**	**95.40% (1431/1500)**
Method 2 (Novel CDAE + Binary CDBN)	100 * 5 for novel CDAE	3 * 5 for Binary CDBN	78.93% (1184/1500)
Method 3 (Novel CDAE + CNN)	100 * 5 for novel CDAE	3 * 5 for CNN	91.07% (1366/1500)
Method 4 (Basic CDAE + Gaussian CDBN)	100 * 5 for basic CDAE	3 * 5 for Gaussian CDBN	89.87% (1348/1500)
Method 5 (Basic CDAE + Binary CDBN)	100 * 5 for basic CDAE	3 * 5 for Binary CDBN	73.93% (1109/1500)
Method 6 (Basic CDAE + CNN)	100 * 5 for basic CDAE	3 * 5 for CNN	86.20% (1293/1500)
Method 7 (Gaussian CDBN)	0 (Without unsupervised initialization)	200 * 5 for Gaussian CDBN	99.07% (1486/1500)
Method 8 (Binary CDBN)	0 (Without unsupervised initialization)	200 * 5 for Gaussian CDBN	78.20% (1173/1500)
Method 9 (CNN)	0 (Without unsupervised initialization)	200 * 5 for Gaussian CDBN	98.33% (1475/1500)
Method 10 (Gaussian CDBN)	0 (Without unsupervised initialization)	100 * 5 for Gaussian CDBN	97.07% (1456/1500)
Method 11 (Binary CDBN)	0 (Without unsupervised initialization)	100 * 5 Binary CDBN	77.60% (1164/1500)
Method 12 (CNN)	0 (Without unsupervised initialization)	100 * 5 CNN	92.73% (1391/1500)
Method 13 (Gaussian CDBN)	0 (Without unsupervised initialization)	50 * 5 for Gaussian CDBN	76.80% (1152/1500)
Method 14 (Binary CDBN)	0 (Without unsupervised initialization)	50 * 5 Binary CDBN	60.40% (906/1500)
Method 15 (CNN)	0 (Without unsupervised initialization)	50 * 5 CNN	73.20% (1098/1500)

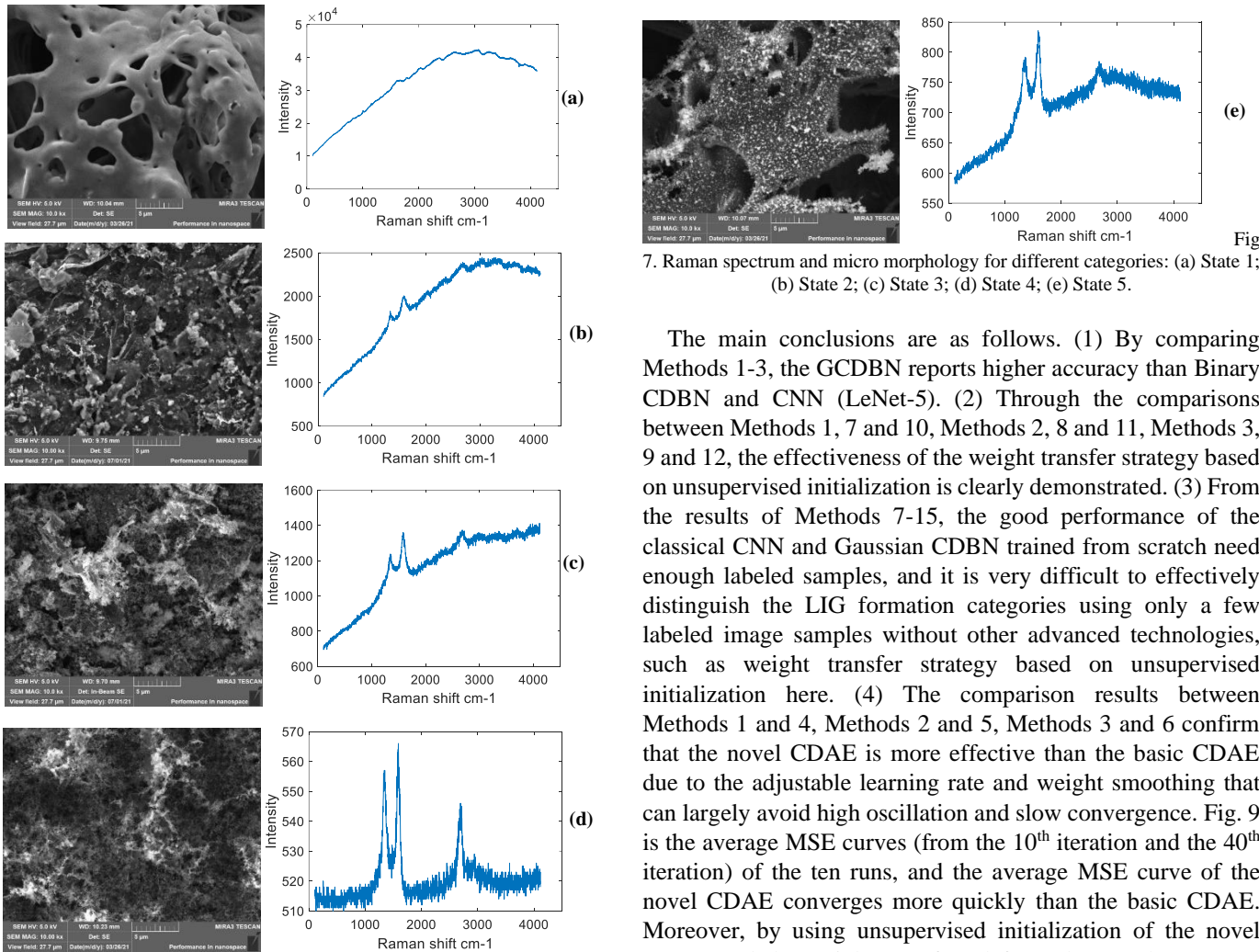**Note: Method 1 refers to the proposed method**

Fig. 7. Raman spectrum and micro morphology for different categories: (a) State 1; (b) State 2; (c) State 3; (d) State 4; (e) State 5.

The main conclusions are as follows. (1) By comparing Methods 1-3, the GCDBN reports higher accuracy than Binary CDBN and CNN (LeNet-5). (2) Through the comparisons between Methods 1, 7 and 10, Methods 2, 8 and 11, Methods 3, 9 and 12, the effectiveness of the weight transfer strategy based on unsupervised initialization is clearly demonstrated. (3) From the results of Methods 7-15, the good performance of the classical CNN and Gaussian CDBN trained from scratch need enough labeled samples, and it is very difficult to effectively distinguish the LIG formation categories using only a few labeled image samples without other advanced technologies, such as weight transfer strategy based on unsupervised initialization here. (4) The comparison results between Methods 1 and 4, Methods 2 and 5, Methods 3 and 6 confirm that the novel CDAE is more effective than the basic CDAE due to the adjustable learning rate and weight smoothing that can largely avoid high oscillation and slow convergence. Fig. 9 is the average MSE curves (from the 10th iteration and the 40th iteration) of the ten runs, and the average MSE curve of the novel CDAE converges more quickly than the basic CDAE. Moreover, by using unsupervised initialization of the novel CDAE and the weight transferred from the novel CDAE to GCDBN, we only need three labeled image samples to achieve high and robust classification performance in this case study. The hyper-parameters and architecture settings used in the proposed method in the case study are listed in **Table IV**.

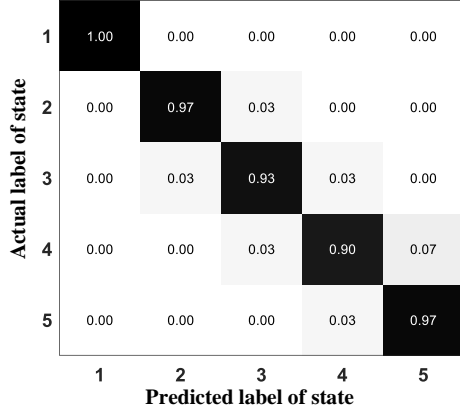| Different methods	Average testing accuracies with different numbers of labeled images for each state					
	1	2	3	4	5	10
Proposed method	**87.47%**	**91.93%**	**95.40%**	**97.73%**	**99.07%**	**100.00%**
SVM	41.80%	60.73%	70.87%	79.47%	84.13%	89.27%

Fig. 8. Confusion matrix of the proposed method (Method 1) for one run.
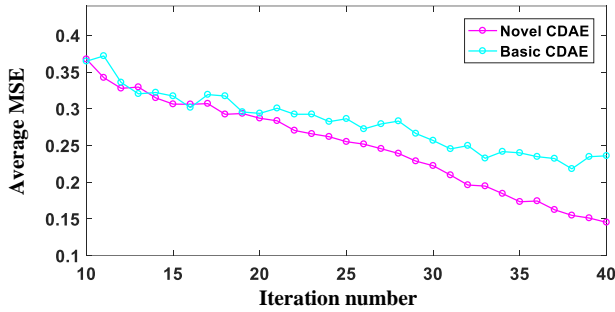

Fig. 9. The average MSE curves of the novel CDAE and basic CDAE.

TABLE IV
HYPER-PARAMETERS AND ARCHITECTURE SETTINGS OF THE NOVEL CDAE AND GAUSSIAN CDBN

Hyper-parameters and architecture settings	Details
The selected 2D size of each grayscale images	40*40
Weight matrices of novel CDAE and Gaussian CDBN in the first convolutional layer	(5*5)*8
Max pooling operations of novel CDAE and Gaussian CDBN in the first pooling layer	(2*2)*8
Weight matrices of novel CDAE and Gaussian CDBN in the second convolutional layer	(5*5)*14
Max pooling operations of novel CDAE and Gaussian CDBN in the second pooling layer	(2*2)*14
Activation functions of novel CDAE and Gaussian CDBN	Sigm
Iteration times of novel CDAE / Gaussian CDBN	100 / 60
Initial learning rate / Noise variance of novel CDAE	0.10 / 0.05

C. Discussions on the size of the labeled images and the noise interference

Generally, acquiring and labeling many in-process monitoring images in practice are laborious and difficult. Thereby, the analysis and discussion on the size of the labeled images for training GCDBN are of significance.

As presented in **Table V**, six different sizes of the labeled images are investigated, which are 1, 2, 3, 4, 5, and 10, respectively. Here, support vector machine, the commonly used

small-sample learning method, is also applied for comparison. For each investigation case, the numbers of the unlabeled images for training novel CDAE and the labeled images for testing GCDBN and SVM are kept at 100 and 30, respectively. It can be found from **Table V** that the average testing accuracies gradually increase with the growing size of labeled images used in the training of GCDBN. Concretely, with only 2 labeled images, the classification accuracy has reached 87%, and with 3 images, the accuracy is higher than 95%. Compared with SVM, the proposed method shows better performance in dealing with extremity small samples with the help of weight transfer strategy based on unsupervised initialization.

Fig. 10 shows the standard deviations of the classification accuracies for each investigation case. It can be observed that the standard deviation shows a steady downward trend as the number of labeled images increases. The proposed method shows excellent capability in LIG formation monitoring with very limited labeled information.
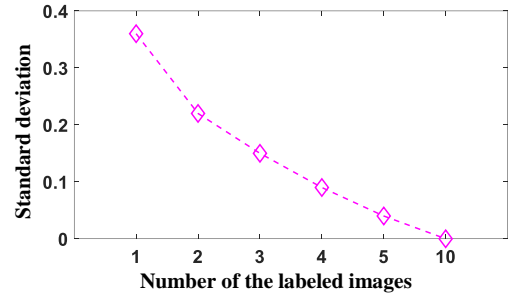

Fig. 10. Standard deviations of the proposed method with different sizes of the labeled images.

To further evaluate the robustness of the proposed method, the influence of noise is analyzed. The noise characteristic is simulated by adding Gaussian white noise with zero-mean and different variances (0.01**I**, 0.03**I**, 0.05**I**, 0.07**I**, and 0.09**I**) into the grayscale images. The grayscale images of the five states with variance 0.01**I** and variance 0.09**I** are shown in Fig. 11 and Fig. 12, respectively.
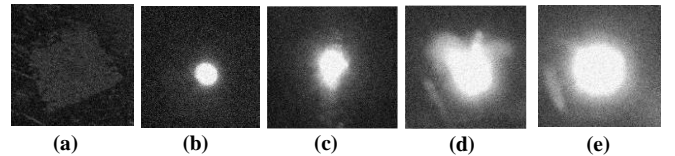

Fig. 11. Grayscale images of five states under Gaussian white noises with variance 0.01**I**: (a-e) States 1, 2, 3, 4, 5. (**I** is the unit matrix)
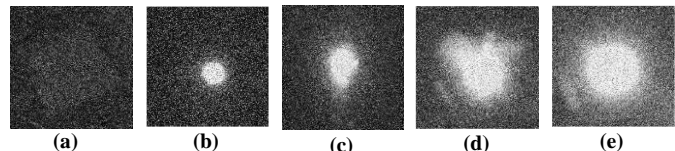

Fig. 12. Grayscale images of five states under Gaussian white noise with variance 0.09**I**: (a-e) States 1, 2, 3, 4, 5. (**I** is the unit matrix)

Here, for different methods, the number of the labeled images is set as 3, the numbers of the unlabeled images for training novel CDAE and the labeled images for testing Gaussian CDBN are always set to 100 and 30, respectively.

For the proposed method and Method 3, their average testing accuracies of the ten runs given under Gaussian white noise with different variance levels are shown in **Table VI**. The detailed accuracies of the proposed method are given in **Fig. 13**. The proposed method is more effective than Method 3 in classifying the original grayscale images under the influence of noise. Besides, despite the average testing accuracies of the proposed method decrease when the variance levels of noise are larger than 0.05, basically, it still shows good anti-noise capability.

TABLE VI
AVERAGE TESTING ACCURACIES UNDER DIFFERENT WHITE NOISE LEVELS

Different methods	Different variances of Gaussian white noise				
	0.01	0.03	0.05	0.07	0.09
Method 1	**94.67%**	**95.17%**	**95.40**%	**94.00%**	**92.67%**
Method 3	91.25%	92.00%	92.67%	90.92%	88.83%

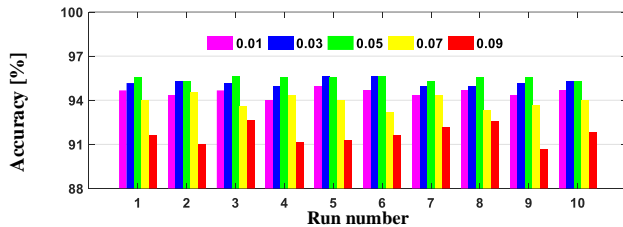**Note: Method 1 refers to the proposed method**

Fig. 13. The detailed testing accuracies of the proposed method.

VI. CONCLUSIONS

Advanced process monitoring of laser-induced graphene manufacturing is of great significance to evaluate the quality of products, improve productivity and reduce material consumption. This paper developed a vision-based intelligent process monitoring system for LIG production. To fully utilize the unlabeled monitoring data and to address the challenge of limited labeled data, novel convolutional networks using unsupervised initialization and weight transfer learning were proposed. First, a novel CDAE was constructed with adjustable learning rate and weight smoothing, which was trained using the unlabeled images to obtain weights containing good knowledge for classification. Then, a GCDBN by employing real-valued input units and hidden units is constructed with the weights transferred from the trained CDAE. Finally, a very small number of labeled images are used to further adjust the weights of the GCDBN. The experimental results showed a superior classification performance compared with state-of-art deep learning methods. The robustness of the proposed methods was also evaluated by varying the labeled data size and corrupting the images with different levels of noise. A possible future work can be exploring multimodal sensory data to achieve more accurate and reliable monitoring with effective sensor fusion.

REFERENCES

[1] X. Wang, Y. Qiu, W. Cao and P. Hu, "Highly Stretchable and Conductive Core–Sheath Chemical Vapor Deposition Graphene Fibers and Their Applications in Safe Strain Sensors", Chemistry of Materials, vol. 27, no. 20, pp. 6969-6975, 2015.

[2] Z. Liu, Z. Wu, S. Yang, R. Dong, X. Feng and K. Müllen, "Ultraflexible In-Plane Micro-Supercapacitors by Direct Printing of Solution-Processable Electrochemically Exfoliated Graphene", Advanced Materials, vol. 28, no. 11, pp. 2217-2222, 2016.

[3] R. Chen, S. Das, C. Jeong, M. Khan, D. Janes and M. Alam, "Co-Percolating Graphene-Wrapped Silver Nanowire Network for High Performance, Highly Stable, Transparent Conducting Electrodes", Advanced Functional Materials, vol. 23, no. 41, pp. 5150-5158, 2013.

[4] O. Akhavan, E. Ghaderi and S. Shirazian, "Near infrared laser stimulation of human neural stem cells into neurons on graphene nanomesh semiconductors", Colloids and Surfaces B: Biointerfaces, vol. 126, pp. 313-321, 2015.

[5] C. Liu, Z. Yu, D. Neff, A. Zhamu and B. Jang, "Graphene-Based Supercapacitor with an Ultrahigh Energy Density", Nano Letters, vol. 10, no. 12, pp. 4863-4868, 2010.

[6] L. Guan, L. Zhao, Y. Wan and L. Tang, "Three-dimensional graphene-based polymer nanocomposites: preparation, properties and applications", Nanoscale, vol. 10, no. 31, pp. 14788-14811, 2018.

[7] H. Bai, C. Li, X. Wang and G. Shi, "On the Gelation of Graphene Oxide", The Journal of Physical Chemistry C, vol. 115, no. 13, pp. 5545-5551, 2011.

[8] X. Cao et al., "Preparation of Novel 3D Graphene Networks for Supercapacitor Applications", Small, vol. 7, no. 22, pp. 3163-3168, 2011.

[9] Z. Bo, K. Yu, G. Lu, P. Wang, S. Mao and J. Chen, "Understanding growth of carbon nanowalls at atmospheric pressure using normal glow discharge plasma-enhanced chemical vapor deposition", Carbon, vol. 49, no. 6, pp. 1849-1858, 2011.

[10] J. Lin et al., "Laser-induced porous graphene films from commercial polymers", Nature Communications, vol. 5, no. 1, 2014.

[11] J. Li, M. Stanford, W. Chen, S. Presutti and J. Tour, "Laminated Laser-Induced Graphene Composites", ACS Nano, vol. 14, no. 7, pp. 7911-7919, 2020.

[12] J. Kanko, A. Sibley and J. Fraser, "In situ morphology-based defect detection of selective laser melting through inline coherent imaging", Journal of Materials Processing Technology, vol. 231, pp. 488-500, 2016.

[13] S. Wang, Y. Wang, C. Liu and J. Mazumder, "In-situ Monitoring on Micro-hardness of Laser Molten Zone on AISI4140 Steel by Spectral Analysis", Scientific Reports, vol. 10, no. 1, 2020.

[14] S. A. Shevchik, G. Masinelli, C. Kenel, C. Leinenbach and K. Wasmer, "Deep Learning for In Situ and Real-Time Quality Monitoring in Additive Manufacturing Using Acoustic Emission," IEEE Transactions on Industrial Informatics, vol. 15, no. 9, pp. 5194-5203, Sept. 2019.

[15] N. Eschner, L. Weiser, B. Häfner and G. Lanza, "Classification of specimen density in Laser Powder Bed Fusion (L-PBF) using in-process structure-borne acoustic process emissions", Additive Manufacturing, vol. 34, p. 101324, 2020.

[16] I. Kao, Y. Hsu, Y. H. Lai and J. Perng, "Laser Cladding Quality Monitoring Using Coaxial Image Based on Machine Learning," in IEEE Transactions on Instrumentation and Measurement, vol. 69, no. 6, pp. 2868-2880, June 2020.

[17] Y. Wang et al., "A CNN-Based Adaptive Surface Monitoring System for Fused Deposition Modeling," IEEE/ASME Transactions on Mechatronics, vol. 25, no. 5, pp. 2287-2296, Oct. 2020.

[18] Y. Zhang, H. G. Soon, D. Ye, J. Y. H. Fuh and K. Zhu, "Powder-Bed Fusion Process Monitoring by Machine Vision With Hybrid Convolutional Neural Networks," IEEE Transactions on Industrial Informatics, vol. 16, no. 9, pp. 5769-5779, Sept. 2020.

[19] X. Li, S. Siahpour, J. Lee, Y. Wang and J. Shi, "Deep Learning-Based Intelligent Process Monitoring of Directed Energy Deposition in Additive Manufacturing with Thermal Images", Procedia Manufacturing, vol. 48, pp. 643-649, 2020.

[20] Y. Feng, Z. Chen, D. Wang, J. Chen and Z. Feng, "DeepWelding: A Deep Learning Enhanced Approach to GTAW Using Multisource Sensing Images," IEEE Transactions on Industrial Informatics, vol. 16, no. 1, pp. 465-474, Jan. 2020.

[21] L. Yang, J. Fan, Y. Liu, E. Li, J. Peng and Z. Liang, "Automatic Detection and Location of Weld Beads With Deep Convolutional Neural

Networks," IEEE Transactions on Instrumentation and Measurement, vol. 70, pp. 1-12, 2021.

[22] H. Shao et al., "Fault Diagnosis of a Rotor-Bearing System Under Variable Rotating Speeds Using Two-Stage Parameter Transfer and Infrared Thermal Images," IEEE Transactions on Instrumentation and Measurement, vol. 70, pp. 1-11, 2021.

[23] X. Gao, C. Zhou, F. Chao, L. Yang, C. Lin, T. Xu, C. Shang and Q. Shen, "A data-driven robotic Chinese calligraphy system using convolutional auto-encoder and differential evolution", Knowledge-based Systems, vol. 182, pp. 104802, 2019.

[24] W. Huang, G. Song, H. Hong and K. Xie, Deep Architecture for Traffic Flow Prediction: Deep Belief Networks With Multitask Learning. IEEE Transactions on Intelligent Transportation Systems, vol. 15, no. 5, pp. 2191-2201, 2014.

[25] X. Lin, H. Shao, H. Jiang, and J. Xiang. Modified Gaussian convolutional deep belief network and infrared thermal imaging for intelligent fault diagnosis of rotor-bearing system under time-varying speeds. Structural Health Monitoring, vol. 21, no. 2, pp. 339-353, 2022.

Min Xia (S'11, M'17, SM'22) is currently a lecturer in the Department of Engineering at Lancaster University, UK. He received B.S. degree in Industrial Engineering from Southeast University, China (2009); M.S. degree in Precision Machinery and Precision Instrumentation from the University of Science and Technology of China, China (2012); and Ph.D. degree in Mechanical Engineering from the University of British Columbia, Canada (2017). His research interests include smart manufacturing, machine diagnostics and prognostics, deep neural networks, wireless sensor network and sensor fusion.

Haidong Shao is currently an Associate Professor in the State Key Laboratory of Advanced Design and Manufacturing for Vehicle Body, College of Mechanical and Vehicle Engineering at Hunan University, Changsha, China. He received the B.S. degree in Electrical Engineering and Automation and the Ph.D. degree in Vehicle Operation Engineering from Northwestern Polytechnical University, Xi'an, China, in 2013 and 2018, respectively. His current research interests include fault diagnosis, and prognostics and health management.

Zheng Huang is currently a PhD student majoring in machinery manufacturing and automation at Wuhan University, China. He received B.S. degree in physics from Chongqing Normal University, China (2016); M.S. degree in physics from Chongqing University, China (2019). His research interests include intelligent manufacturing, low dimensional materials and their applications, electronic devices.

Zhe Zhao is currently a graduate student in the Institute of Technological Sciences of Wuhan University, China. He received B.S. degree in Energy and Power Engineering from Wuhan University of technology, China (2020).His research interests includes Laser Advanced Manufacturing, in situ monitoring of dissimilar metal additive manufacturing .

Feilong Jiang is currently a graduate student in the Institute of Technological Sciences of Wuhan University, China. He received B.S. degree in Mechanical Design manufacture and Automation from Wuhan University, China (2020). His research interests include industrial application of lasers, deep neural networks, and physics informed neural network.
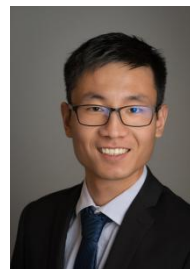
Yaowu Hu is currently a professor in The Institute of Technological Sciences at Wuhan University, China. He received B.S. degree in Engineering Mechanics from Southeast University, China (2009); M.S. degree in Advanced Manufacturing from Institute of Mechanics, Chinese Academy of Sciences, China (2012); and Ph.D. degree in Industrial Engineering from Purdue University, USA(2016). His research interests include advanced manufacturing, laser processing, micro/nano fabrication and mechanics.